ORIGINAL ARTICLE

lajss.org© Latin American Journal of Solids and Structures

www.lajss.org

Numerical Evaluation of Dynamic Constitutive Models and Modified Analytical Modeling for High-Velocity Penetration of Ultra-High-Performance Concrete (UHPC)

Yalong Wang[a], Wenbin Li[a*], Guixiang Yin[b], Zhongqiang Cheng[c], Yiming Li[a], Kun Zhang[a], Ronghua Ma[a]

[a] School of Mechanical Engineering, Nanjing University of Science and Technology, Nanjing 210094, Jiangsu, China. Email: wangyalong@njust.edu.cn, lwb2000cn@njust.edu.cn, Liyiming0919@163.com, 223101031250@njust.edu.cn, mrh@njust.edu.cn

[b] Mongolia Research Institute of Metallic Materials, Yantai 264000, Shandong, China. Email: dzsygx@163.com

[c] Jiangnan Industries Group Co., LTD. Xiangtan 411207, Hunan, China. Email: 410857563@qq.com

* Corresponding author

https://doi.org/10.1590/1679-7825/e9207

Abstract

This study evaluates and improves models for predicting the high-velocity penetration response of ultra-high-performance concrete (UHPC) used in protective structures. The research scope involves systematically comparing three common concrete constitutive models: Holmquist–Johnson–Cook (HJC), Riedel–Hiermaier–Thoma (RHT), and Karagozian & Case (K&C). First, the models' theoretical differences regarding strain-rate effects and tension-compression asymmetry were analyzed. Next, their material parameters were calibrated using fundamental mechanical tests and literature data. An LS-DYNA finite element model was then established and validated against ballistic experiments (633-959 m/s) by evaluating penetration depth, surface crater morphology, and internal damage evolution. The results indicate that the HJC model is the optimal choice for high-velocity penetration simulations. It yielded the lowest average depth error (-11.89%), and its localized damage pattern best matched UHPC's high-strength and high-toughness traits. In contrast, the RHT model caused premature matrix softening under high hydrostatic pressure, leading to a -21.76% error. The K&C model overpredicted surface funnel-shaped crater damage, with its penetration depth error increasing to -26.34% at high velocities. Furthermore, extended simulations at 800–1500 m/s revealed that the traditional Forrestal analytical model deviates significantly in the ultra-high-velocity regime. To solve this, a modified analytical model tailored for UHPC was developed. By accounting for dynamic yield and high-pressure shear rheological softening mechanisms, the new model introduces a dynamic strengthening coefficient and a rheological softening factor. Ballistic validation demonstrates that, within the validated range, the theoretical predictions of this modified model match the experimental data well, with a maximum relative error of 14.54%. Overall, this research provides reliable numerical model selection and theoretical support for designing and evaluating UHPC protective structures against kinetic energy projectile impacts.

Keywords

UHPC, High-Velocity Penetration, Depth of Penetration, HJC model, RHT model, K&C model, Dynamic cavity-expansion theory, Numerical Simulation.

Graphical Abstract

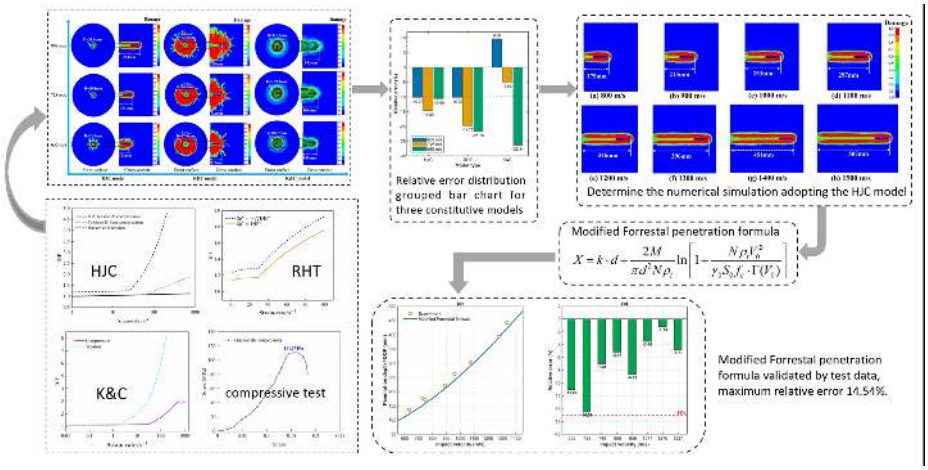

Received July 22, 2026. In revised form August 16, 2026. Accepted August 23, 2026. Available online August 25, 2026.
https://doi.org/10.1590/1679-7825/e9207

Latin American Journal of Solids and Structures. ISSN 1679-7825. Copyright © 2026. This is an Open Access article distributed under the terms of the Creative Commons Attribution License, which permits unrestricted use, distribution, and reproduction in any medium, provided the original work is properly cited.

1 INTRODUCTION

Ultra-high-performance concrete (UHPC) is widely utilized in military protective structures and critical infrastructure. Specifically, Liu et al. (2022) comprehensively reviewed the application of UHPC targets against high-velocity projectile impacts. Experimental evaluations by Yu et al. (2016) demonstrated its exceptional energy absorption capacity under dynamic modes, while Lai et al. (2014) highlighted its superior durability and properties under direct penetration and explosion. Under high-strain-rate impact, UHPC exhibits a pronounced strain-rate effect. Bragov et al. (2013) evaluated the dynamic strengths and toughness of these materials, and Hu et al. (2023) further confirmed this dynamic performance through systematic split Hopkinson pressure bar (SHPB) testing. Due to high volume fractions of short steel fibers, crack propagation within the matrix is strongly inhibited by fiber bridging and dynamic pull-out mechanisms. Yang et al. (2022) analyzed how different steel fiber volume contents and types influence tensile stress-strain behavior, whereas Du et al. (2009) verified the high dynamic toughness through fundamental mechanical property tests. Furthermore, with a sudden surge in strain rate, the failure mode of UHPC transitions from localized cracking to global, continuous energy-dissipating pulverization. Regarding this phenomenon, Han et al. (2024) explored the dynamic fracture mechanisms under such conditions. Liu (2023) investigated the effect of hybrid fibers on these dynamic mechanical properties. Li et al. (2024) analyzed the influence of fiber morphology on dynamic compressive properties under one-dimensional stress waves, while Yu et al. (2021) summarized the research progress on dynamic compressive behavior at high strain rates. Additionally, Dong et al. (2026) studied the mechanical-electric response characteristics of UHPC-based composites under impact loading. This complex multi-scale, non-linear dynamic response complicates the accurate characterization of its constitutive relationships under extreme loading, presenting a critical theoretical bottleneck. Addressing this, Guo et al. (2018) developed a constitutive model for low-velocity impact simulations, and Zhou et al. (2023) proposed a novel dynamic constitutive model specifically for projectile impact scenarios.

Numerical simulation is an efficient approach to evaluate localized impact damage, where the selection and calibration of constitutive models determine computational fidelity. Das and Nanthagopalan (2024) demonstrated this through a comprehensive parametric analysis of ballistic impact resistance, and Yang et al. (2021) emphasized the importance of accurate constitutive modeling under impact and blast loadings. In LS-DYNA, three continuum dynamic models are predominantly used for concrete-like materials: the Holmquist–Johnson–Cook (HJC) model (Holmquist et al. 1993), the Riedel–Hiermaier–Thoma (RHT) model (Riedel et al. 1999), and the Karagozian & Case (K&C) model (Malvar et al. 1997).

Beyond impact and blast engineering, nonlinear finite element analysis has been widely applied to the integrity assessment of internally pressurized structures, in which an accurate constitutive description of material nonlinearity is equally decisive. Pany (2021a) employed an inverse Ramberg-Osgood relation to represent the stress-strain behavior of high-strength low-alloy (HSLA) 15CDV6 steel and combined elasto-plastic finite element analysis with experimental stress analysis to estimate the failure pressure of a pressurant tank, revealing that structural discontinuity and long-seam mismatch induce pronounced stress concentration. Pany (2021b) further demonstrated through nonlinear finite element analysis that profile deviations of cylindrical pressure-vessel shells elevate local stresses and reduce the safety margin relative to the material yield strength. Pany (2022) performed nonlinear (geometric and material) finite element analyses of circular, elliptical, and obround pressure vessels under internal pressure, showing that non-circular cross-sections undergo non-uniform bending with higher effective stresses. These studies consistently confirm that the fidelity of structural failure predictions relies on both accurate material constitutive modeling and proper treatment of geometric discontinuities, a requirement equally critical to the dynamic constitutive characterization of UHPC in high-velocity penetration simulations.

Extensive studies have evaluated these models for conventional concrete under penetration and blast scenarios. For instance, Sun et al. (2016) investigated the parameters of the HJC model for reinforced concrete perforation. Ma et al. (2019) conducted numerical evaluations of target resistance against high-velocity projectiles, and Wang et al. (2007) analyzed crater damage evolution utilizing ogive-nose steel projectiles. However, because they were developed for conventional concrete, their governing equations cannot explicitly represent the meso-scale toughening mechanisms of UHPC. Zou et al. (2023) highlighted the specific role of fiber bridging in enhancing interface toughness, while Su et al. (2022) attempted to address these gaps by calibrating the K&C model specifically for UHPC. Researchers have also calibrated these traditional models for UHPC under contact explosions or low-to-medium velocity scenarios. Wan et al. (2021) determined the HJC parameters for steel-fiber UHPC. Song et al. (2023) further applied the HJC model to ultra-high performance concrete, and Du et al. (2025) systematically researched the strain rate effects across three dynamic models. Additionally, Zhou et al. (2023) proposed a novel dynamic constitutive model for UHPC under projectile impact, and Yan et al. (2025) evaluated the suitability of high-pressure dynamic constitutive models. Despite these efforts, their applicability in high-to-hyper velocity penetration (≥800 m/s) remains largely unexplored.

At such extreme velocities, intensive compression violently forces the target medium into a highly densified, fluid-like hydrodynamic stress state under surging hydrostatic pressure. Wang and Qian (2004) established the scale conversion relationship for projectile penetration and perforation into concrete media, Wang et al. (2006) proposed an anti-penetration calculation method for steel-fiber ultra-high-strength reactive powder concrete (RPC), and Forrestal and Tzou (1997) developed a spherical cavity-expansion penetration model for concrete targets. This extreme environment severely challenges the volumetric equation of state (EOS), the dynamic increase factor (DIF), and the shear softening terms of traditional models. Riedel et al. (1999) numerically analyzed the penetration of reinforced concrete by the BETA-B-500 projectile using a new macroscopic concrete model for hydrocodes, whereas Rong et al. (2010) investigated the anti-penetration behavior of ultra-high-performance steel-fiber-reinforced concrete (UHPFRC) through numerical simulation. Currently, scant literature systematically addresses their accuracy and numerical stability discrepancies in predicting localized cratering topology, deep-tunnel resistance, and energy dissipation pathways for homogeneous UHPC under hyper-velocity rigid projectile impacts; among the few exceptions, Wan et al. (2021) determined and evaluated the HJC parameters for steel-fiber-reinforced UHPC, and Song et al. (2023) determined and applied the HJC parameters for ultra-high-performance concrete.

Despite the abovementioned contributions, several critical research gaps remain. First, existing calibration studies of the HJC, RHT, and K&C models for UHPC were mostly conducted under quasi-static, low-, or medium-velocity loading, leaving their predictive performance under high-to-hyper velocity penetration (≥800 m/s) largely unexamined. Second, no comprehensive benchmarking has compared these three models within a unified numerical framework regarding penetration depth, crater morphology, and internal damage evolution under identical conditions. Third, classical analytical models, such as the Forrestal cavity-expansion model, have not been modified to account for the dynamic strengthening and high-pressure shear rheological softening of UHPC in the ultra-high-velocity regime. These gaps motivate the present study.

To fill these research gaps, this study presents a comprehensive numerical and analytical investigation. First, the HJC, RHT, and K&C constitutive models are calibrated and benchmarked against ballistic tests in LS-DYNA to determine the optimal numerical framework. Hyper-velocity simulations are then executed to elucidate the coupled high-pressure and high-strain-rate response mechanisms of UHPC, exposing the limitations of classical analytical models during high-velocity extrapolation. Finally, a modified analytical model incorporating a high-pressure correction coefficient is formulated based on Forrestal resistance theory and rigorously validated using multi-velocity experimental data.

2 Theoretical Comparison of Strain-Rate Effects among Three Constitutive Models

During the dynamic process of high-velocity projectile penetration into ultra-high-performance concrete (UHPC), the target material is subjected to extreme states of high hydrostatic pressure, elevated strain rates ($10^3 \sim 10^4\ \mathrm{s}^{-1}$), and intense shear damage evolution (Pham et al. 2024; Blasone et al. 2021; Zhou et al. 2024). Under severe dynamic loading, ultra-high-performance concrete (UHPC) exhibits pronounced strain-rate sensitivity; thus, the strain-rate effect must be incorporated into numerical simulations (Du et al. 2025). The dynamic increase factor (DIF) is commonly employed to characterize the variation laws of material strength under varying strain rates (Fan et al. 2023). From the perspectives of mathematical constitutive equations and physical mechanisms, this chapter systematically compares the similarities and differences among the HJC, RHT, and K&C models regarding the formulation of strength failure surfaces, strain-rate effect characterization, and volumetric equations of state (EOS). Particular emphasis is placed on critically dissecting the inherent theoretical limitations and applicable boundaries of these three models when handling high-pressure hydrodynamic regimes induced by projectile erosion.

2.1 HJC Constitutive Model and Strain-Rate Effect Characterization

The HJC constitutive model has become a widely adopted model for penetration and blast simulations, owing to its concise parameter set, its capability to comprehensively capture the non-linear volumetric compression, hydrostatic pressure hardening, and strain-rate effects of concrete, and its early implementation as a built-in model in LS-DYNA. Sun et al. (2016) investigated the HJC model parameters in simulating the perforation experiments of reinforced concrete; Polanco-Loria et al. (2008) predicted the ballistic limits of concrete slabs using a modified version of the HJC model; and Zhou et al. (2023) analyzed the performance of a reinforced concrete structure subjected to a high-velocity large-caliber projectile. The HJC model primarily comprises three core components: the yield surface, the equation of state (EOS), and the damage evolution equation. Specifically, the governing equation of the model yield surface is expressed as Eq. (1), and the formulation for calculating the dynamic increase factor (DIF) is given in Eq. (2).

$$\sigma^* = \left[A(1-D) + BP^{*N}\right]\left(1 + C\ln\dot{\varepsilon}^*\right) \tag{1}$$

$$DIF = \frac{f_d}{f_s} = 1 + C\ln\dot{\varepsilon}^* \tag{2}$$

Where $\sigma^* = \sigma/F_c$ *denotes the dimensionless equivalent stress, and* $P^* = p/F_c$ *denotes the dimensionless hydrostatic pressure;* F_c *is the static uniaxial compressive strength, and p stands for hydrostatic pressure.* $\dot{\varepsilon}^*$ *refers to the ratio of the actual strain rate* $\dot{\varepsilon}$ *to the reference strain rate* $\dot{\varepsilon}_0$, A, B, N are strength parameters of the material model; D is the damage variable; C represents the strain rate coefficient. f_d and f_s denote the dynamic strength and quasi-static strength of concrete, respectively.

A vast number of experiments have demonstrated that the strain-rate sensitivity of concrete differs significantly between tensile and compressive states, and its dynamic increase factor (DIF) curves exhibit distinct critical inflection points. Wang et al. (2022) derived the dynamic increase factors of concrete-like materials at very high strain rates; Khan and Iqbal (2024) experimentally investigated the strain-rate and size effects on the dynamic tensile behavior of standard and high-strength concrete; Tedesco and Ross (1998) proposed strain-rate-dependent constitutive equations for concrete; and Hassan and Wille (2022) measured the direct tensile behavior of steel-fiber-reinforced UHPC at high strain rates using a modified split Hopkinson tension bar. Under high-strain-rate loading, the enhancement in uniaxial compressive strength can exceed twofold, whereas the increase in uniaxial tensile strength can reach up to sixfold (Li et al. 2025; Yang et al. 2018). Once the loading rate surpasses a critical threshold, the growth rate of the DIF accelerates sharply. This pronounced tension–compression asymmetry implies that the rate effects under dynamic tension and compression must be independently characterized when formulating constitutive models.

However, in non-linear numerical simulations of intense impacts, the strain-rate formulation of the traditional HJC constitutive model possesses an inherent deficiency (Wan et al. 2021; Du et al. 2025): this model solely employs a single logarithmic relationship, i.e., $DIF = 1 + C\ln\dot{\varepsilon}^*$, to uniformly describe the dynamic strength enhancement effects under both tensile and compressive loading conditions. Figure 1 illustrates a comparison of the DIF curve predicted by the traditional HJC model against the dynamic compression model proposed by Tedesco and Ross (1998) and the dynamic tensile model established by Hassan and Wille (2022) based on split Hopkinson tensile bar (SHTB) tests, wherein the rate sensitivity coefficient of the HJC model adopts the constant C=0.019 calibrated by Wan et al. (2021). Graphical and analytical observations reveal that the DIF curve corresponding to the HJC model varies linearly as a single straight line in semi-logarithmic coordinates and lacks the inflection threshold observed in experiments, which is highly inconsistent with the other two sets of measured experimental data presented in Figure 1.

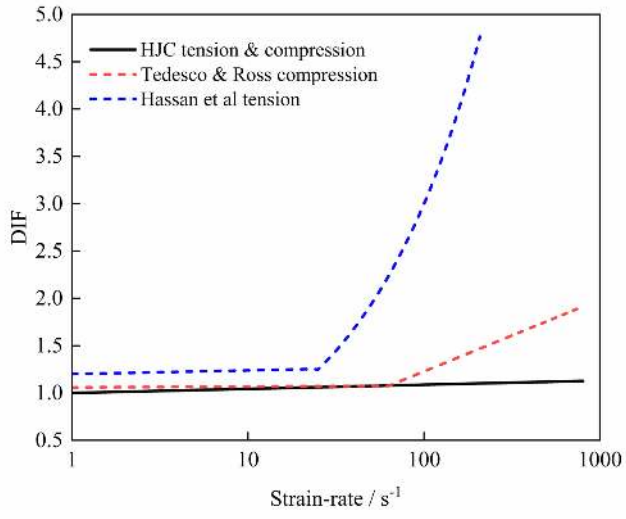

Figure 1: Comparison of HJC model DIF curves

2.2 Theoretical Formulation and Strain-Rate Effect Characterization of the RHT Model

The RHT constitutive model comprises three core components: the limit surface equation, the equation of state (EOS), and the damage equation. The limit surfaces of this model encompass the elastic limit surface, the failure surface, and the residual failure surface (Du et al. 2025). The RHT model introduces a rate function into the failure surface equation to characterize the strain-rate effect of concrete, and the dynamic enhancement expression of the failure surface is formulated as Eq. (3):

$$Y_{fail}(P^*,\theta,\dot{\varepsilon}_p) = F_{rate}^{N+1} Y_{original}\left(\frac{P}{F_{rate}},\theta\right) \tag{3}$$

Where Y_{fail} denotes the failure surface strength under dynamic loading, θ is the stress Lode angle, and $\dot{\varepsilon}_p$ represents the equivalent plastic strain rate. F_{rate} is the strain rate enhancement function, and Y_{original} refers to the original failure surface strength under quasi-static conditions.

The dynamic increase factor (DIF) is equivalent to the rate function, which is defined as:

$$DIF = \frac{f_d}{f_s} = F_{rate}(\dot{\varepsilon}_p, p) \tag{4}$$

Where $F_{rate}\left(\dot{\varepsilon}_p, p\right)$ is a piecewise function that separately characterizes the rate-dependent mechanical responses of materials under tension and compression, while coupling the combined effects of strain rate and hydrostatic pressure. The RHT model (LS-DYNA, 2017) accounts for the influence of hydrostatic pressure, and adopts a piecewise function to describe the variation law of the dynamic increase factor (DIF) with strain rate and normalized hydrostatic pressure p^*, as expressed in Eq. (5):

$$DIF(\dot{\varepsilon}, p^*) = \begin{cases} \mathrm{DIF}^c & 3p^* \geq \mathrm{DIF}^c \\ \mathrm{DIF}^c - \dfrac{3p^* - \mathrm{DIF}^c}{\mathrm{DIF}^c + \mathrm{DIF}^t f_t^*}\left(\mathrm{DIF}^t - \mathrm{DIF}^c\right) & \mathrm{DIF}^c > 3p^* \geq -\mathrm{DIF}^t f_t^* \\ \mathrm{DIF}^t & -\mathrm{DIF}^t f_t^* > 3p^* \end{cases} \tag{5}$$

Where $f_t^* = f_t/f_c$ denotes the dimensionless static tensile strength, and f_t is the static uniaxial tensile strength of the material; DIF^c and DIF^t represent the dynamic increase factors under pure compression and pure tension, respectively.

The compressive dynamic increase factor DIF^c and tensile dynamic increase factor DIF^t are defined in a bilinear piecewise form, with their formulations shown in Eq. (6). This bilinear rate-dependent formulation was originally established in the RHT model documented in the LS-DYNA user manual (LS-DYNA, 2017). Sauer et al. (2017) employed this formulation in developing a validated hydrocode model for adobe under impact loading, and Luccioni et al. (2018) adopted it in the experimental and numerical analysis of the blast response of high-strength fiber-reinforced concrete slabs. In addition, Liu and Li (2019) examined the strain-rate effect on the compressive strength of brittle materials and incorporated the corresponding rate-dependent formulation into a material strength model.

$$\begin{cases} \mathrm{DIF}^c(\dot{\varepsilon}) = \begin{cases} \left(\dfrac{\dot{\varepsilon}}{\dot{\varepsilon}_0^c}\right)^{\beta_c} & \dot{\varepsilon} \leq 30\ \mathrm{s}^{-1} \\ \gamma_c \sqrt[3]{\dot{\varepsilon}} & \dot{\varepsilon} > 30\ \mathrm{s}^{-1} \end{cases} & \text{for compression} \\ \mathrm{DIF}^t(\dot{\varepsilon}) = \begin{cases} \left(\dfrac{\dot{\varepsilon}}{\dot{\varepsilon}_0^t}\right)^{\beta_t} & \dot{\varepsilon} \leq 30\ \mathrm{s}^{-1} \\ \gamma_t \sqrt[3]{\dot{\varepsilon}} & \dot{\varepsilon} > 30\ \mathrm{s}^{-1} \end{cases} & \text{for tension} \end{cases} \tag{6}$$

where $\beta_c = \frac{4}{20+3f_c}$, $\beta_t = \frac{2}{20+f_c}$, and the unit of f_c is MPa; $\log\gamma_c = 6\beta_c - 0.492, \log\gamma_t = 7\beta_t - 0.492$; The reference strain rate for compression is $\dot{\varepsilon}_0^c = 3.0 \times 10^{-5}\ \mathrm{s}^{-1}$, and the reference strain rate for tension is $\dot{\varepsilon}_0^t = 3.0 \times 10^{-6}\ \mathrm{s}^{-1}$.

Figure 2 presents the DIF growth curves under various hydrostatic pressures. When the dimensionless hydrostatic pressure P^* falls within the interval $[-f_t^* \cdot \mathrm{DIF}^t/3,\ \mathrm{DIF}^c/3]$, the material DIF is obtained by interpolation between the two characteristic curves for compression and tension.

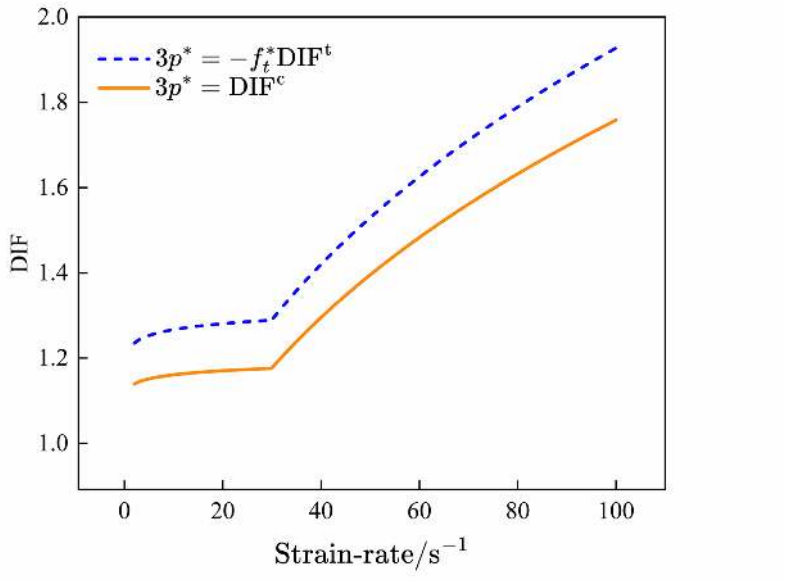

Figure 2: DIF growth curves of the RHT model under varying hydrostatic pressures

Since the elastic limit surface equation of the RHT model is derived from its failure surface equation, the strain-rate effect is implicitly incorporated into the elastic limit surface. Compared with the HJC model, which merely employs a single logarithmic function and fails to distinguish the discrepancies between tensile and compressive rate effects or capture inflection features, the RHT model provides a more precise and detailed theoretical formulation that can reproduce the experimental phenomenon of piecewise inflection points in the DIF growth curves (Wang et al. 2022; Grote et al. 2001).

2.3 Theoretical Formulation and Strain-Rate Effect Characterization of the K&C Model

The K&C constitutive model comprises three sets of limit surface equations and a damage evolution equation. Compared with the RHT model, it simultaneously incorporates strain-rate effects into both the failure surface equation and the damage equation, with the core expression given as Eq. (7):

$$\begin{cases} \Delta\sigma_e = r_f \Delta\sigma\left(\dfrac{p}{r_f}\right) & \text{The adjusted limit surface} \\ \lambda = \begin{cases} \displaystyle\int_0^{\bar{\varepsilon}_p} \frac{d\bar{\varepsilon}_p}{\gamma_f\left[1+\dfrac{p}{\gamma_f f_t}\right]^{b_1}},\ p \geq 0 & \text{Damage by tension} \\ \displaystyle\int_0^{\bar{\varepsilon}_p} \frac{d\bar{\varepsilon}_p}{\gamma_f\left[1+\dfrac{p}{\gamma_f f_t}\right]^{b_2}},\ p \leq 0 & \text{Damage by compression} \end{cases} \end{cases} \tag{7}$$

Where: λ denotes the damage function, $\Delta\sigma_e$ is the failure surface corrected by dynamic hardening, and r_f represents the dynamic increase factor (DIF). This model adopts the radial scaling method to characterize the strain-rate hardening behavior of concrete, which enables direct calibration of DIF evolution curves under various tension and compression loading conditions using experimental data.

The original K&C model adopts the DIF calculation formulation recommended by the Euro-International Committee for Concrete (CEB) (Comité Euro-International du Béton, 1993), which was fitted based on split Hopkinson pressure bar (SHPB) test data (Liu and Li 2019), as expressed in Eq. (8):

$$\mathrm{DIF}(\dot{\varepsilon}) = \begin{cases} \left(\dfrac{\dot{\varepsilon}}{\dot{\varepsilon}_S}\right)^{1.026\alpha_S} & \text{for } \dot{\varepsilon} \le 30\ \mathrm{s}^{-1} \\ \gamma_S \left(\dfrac{\dot{\varepsilon}}{\dot{\varepsilon}_S}\right)^{\frac{1}{3}} & \text{for } \dot{\varepsilon} > 30\ \mathrm{s}^{-1} \end{cases} \tag{8}$$

Where: $\alpha_S = 1/(5 + 9f_c/f_{c0})$, $\gamma_S = 10^{(6.156\alpha_S - 2.0)}$; the reference strain rate $\dot{\varepsilon}_S = 3.0 \times 10^{-5}\ \mathrm{s}^{-1}$; the reference compressive strength $f_{c0} = 10$ MPa; f_c denotes the static compressive strength of the material in MPa. This formula is a bilinear piecewise function plotted in logarithmic coordinates, with a critical strain rate of $30\ \mathrm{s}^{-1}$. Once the strain rate exceeds this critical threshold, the DIF value rises rapidly with increasing strain rate. The updated K&C model introduces an upper cutoff value of 2.94: when the strain rate exceeds $300\ \mathrm{s}^{-1}$, the DIF value is capped at this threshold (Tu and Lu 2009; Kong et al. 2017; LS-DYNA, 2017).

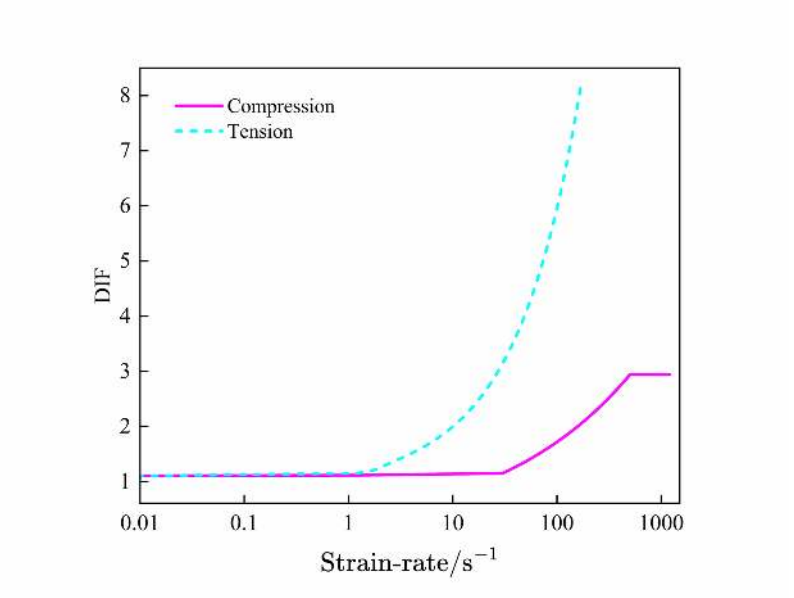

Figure 3: DIF curves of the K&C model

Figure 3 illustrates the dynamic increase factor (DIF) variation curves of the K&C model. The evolution trend of the curves indicates that once the strain rate surpasses the inflection point, the dynamic strengthening effect of the concrete material is significantly enhanced, which agrees closely with the empirical trends observed in dynamic loading tests of concrete.

2.4 Comparison of Strain-Rate Effects among Three Constitutive Models

In summary, although all three dynamic constitutive models characterize strain-rate effects via the dynamic increase factor (DIF), distinct discrepancies exist in their theoretical formulations: the HJC model utilizes a natural logarithmic function; the RHT model adopts a piecewise power function; whereas the K&C model constructs a strain-rate-dependent relationship anchored to experimental data.

From the perspective of accuracy and completeness in describing rate dependency, the theoretical framework of the HJC model is relatively simplified and fails to differentiate between the tensile and compressive mechanical behaviors of the material. Its DIF curve exhibits a continuous, non-piecewise linear trend in semi-logarithmic coordinates, which deviates significantly from empirical observations. In contrast, the RHT and K&C models provide more accurate descriptions of the strain-rate effects in concrete; both models independently characterize the tensile and compressive behaviors and define the DIF using piecewise formulations.

However, when these standard models are directly applied to UHPC modeling, several inherent limitations must be recognized. The HJC model, with its single logarithmic DIF formulation and simple damage accumulation, cannot reproduce the pronounced nonlinear rate strengthening of UHPC at extremely high strain rates, nor can it capture the fiber-bridging-induced ductility and toughness. The RHT model, although distinguishing tensile and compressive rate effects, tends to over-soften the matrix under high hydrostatic pressure, which may underestimate the penetration resistance in the deep-tunneling stage. The K&C model, which relies heavily on user-defined strain-rate curves and a specific λ-η damage function, generally overestimates the surface funnel-shaped crater while underestimating the deep-tunnel resistance. These limitations motivate the systematic parameter re-calibration and the subsequent analytical model modification presented in this paper.

3 UHPC Material Parameter Determination and Numerical Validation of Penetration

To eliminate non-physical artifacts inherent in trial-and-error calibration, this section establishes a rigorous numerical framework for C120-grade UHPC penetration dynamics. First, the constitutive parameters for the HJC, RHT, and K&C models are systematically calibrated. Next, an LS-DYNA mesh convergence analysis is performed to isolate geometric and wave reflection effects. Finally, the models are benchmarked against ballistic experimental data to analyze their mechanistic discrepancies and identify the optimal configuration for high-velocity resistance simulations.

3.1 Parameter Determination of the Three Dynamic Constitutive Models

To improve the transparency of the parameter selection, a sensitivity-guided, two-level stepwise calibration strategy was adopted. Given the large number of parameters in the three models (21 for the HJC model and even more for the RHT and K&C models) and the limited high-pressure experimental data available for UHPC, a fully simultaneous identification of all parameters is not well-posed; therefore, only the core parameters that significantly influence the penetration response were optimized, while the insensitive or directly measured parameters were fixed. On the first level, the core parameters were treated as unknowns and determined by stepwise minimization against experimental data: the yield-surface parameters (A, B, and N) were obtained by least-squares minimization of the normalized sum of squared errors between the fitted and measured yield stresses over the triaxial compression data (Wu 2019); the strain-rate parameters (C for the HJC model; β_t and β_c for the RHT model) were calibrated by minimizing the deviation of the predicted DIF from the measured dynamic strength data under varying strain rates (Wan et al. 2021; Du et al. 2025); and the damage parameters were identified through iterative numerical trials and inverse minimization of the discrepancy between the simulated and measured uniaxial compressive stress-strain responses. On the second level, the remaining parameters were held fixed: the basic physical parameters (e.g., density, compressive and tensile strengths, elastic modulus, and Poisson's ratio) were directly determined from the fundamental material tests of UHPC (Figure 4), and the parameters that cannot be uniquely identified from the available data (e.g., the high-pressure equation-of-state parameters) were adopted from well-established literature values. Previous parameter-sensitivity analyses of the HJC model (Chen et al. 2012) have demonstrated that the predicted penetration response is dominated by the yield-surface, strain-rate, and damage parameters identified above, whereas moderate variations of the remaining parameters within their literature ranges have only a minor influence on the predicted depth of penetration. In this way, every parameter is either physically measured, optimized against experimental evidence, or verified to have a secondary influence, which ensures that the calibration is based on a rigorous optimization/minimization process that thoughtfully considers all parameters.

To ensure the reliability of the numerical simulation results, this study integrates the baseline mechanical tests of UHPC with relevant literature on intense impact dynamics to complete the calibration of the core parameters for the three dynamic constitutive models, namely, the HJC, RHT, and K&C models.

The HJC constitutive model comprises a total of 21 parameters. The density ρ and compressive strength F_c are obtained from the baseline material tests of UHPC, as illustrated in Figure 4. From the quasi-static stress-strain curve in Figure 4(a), C120 (nominal compressive strength of 120 MPa) ultra-high-performance concrete exhibits an initial linear-elastic response. It reaches a peak compressive strength of 111.3 MPa, followed by post-peak stress softening. Figures 4(b) and 4(c) illustrate the specimen states before and after the compression test, respectively; compared with the intact specimen, the failed specimen retains its overall integrity with only a few fine surface cracks, which is attributable to the fiber bridging effect and the dense matrix of the C120 UHPC. This behavior is consistent with its dense matrix and fiber-reinforced material characteristics. Based on the triaxial compression test data of UHPC provided by Wu (2019), curve fitting is performed on Eq. (1) using the least-squares method to determine the normalized cohesive strength A, the normalized pressure hardening coefficient B, and the pressure hardening exponent N. The strain-rate coefficient C is derived from the compressive strength test results of UHPC under varying strain rates (Wan et al. 2021).

The remaining parameters are determined with reference to the existing literature. Song et al. (2023) determined and applied the HJC constitutive model parameters specifically for UHPC. Du et al. (2025) investigated the strain-rate effect of three dynamic constitutive models for UHPC. In addition, Chen et al. (2012) conducted a numerical simulation study on the parameter sensitivity of the concrete HJC model, and Jiang et al. (2012) investigated the high-pressure state equation of high-strength concrete through gas-gun experiments. The complete set of parameters for the HJC constitutive model is summarized in Table 1.

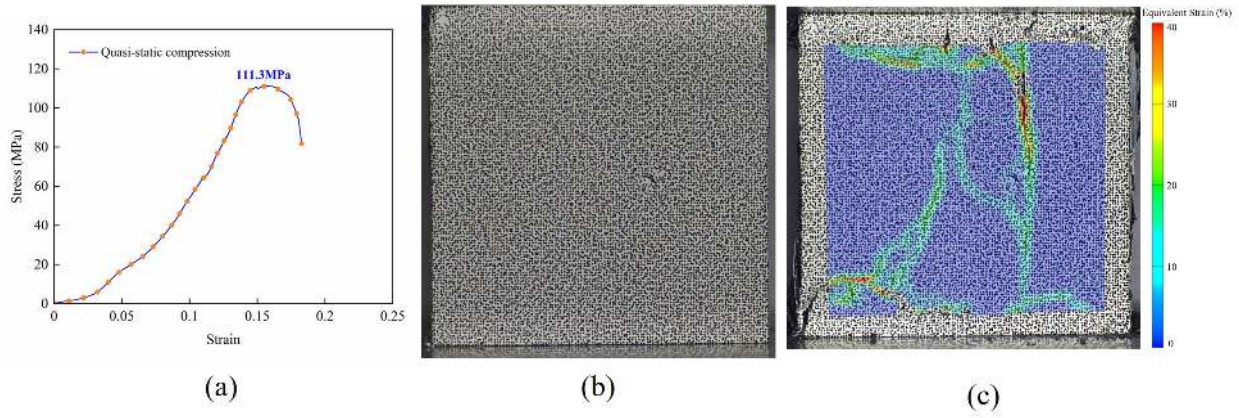

Figure 4: Quasi-static compression test of the C120 UHPC: (a) stress-strain curve with salient features (peak compressive strength f_c, peak strain ε_c, and post-peak softening behavior); (b) pre-compression state; (c) post-compression damage state.

Table 1 Summary of mechanical parameters for the HJC concrete constitutive model

Yield surface parameters		Damage parameters		Equation of state parameters		Basic material parameters	
A	0.3	ε_{EFMIN}	0.0018	P_c	35.0MPa	F_c	111.3MPa
B	1.781			P_1	235.0MPa		
N	0.81	D_1	0.063	μ_c	0.0011	G	20.37GPa
C	0.019			μ_l	0.0383		
T	11.68MPa	D_2	1.0	K_1	46.4GPa	ρ	2.54 g·cm-3
S_{FMAX}	3.5			K_2	-195.0GPa		
				K_3	416.6GPa		

The RHT model adopts a decoupled configuration, separately defining the elastic limit surface and the residual failure surface, and incorporates mutually independent exponent parameters for the tensile and compressive strain-rate effects. Given the numerous parameters involved in this model and the limited availability of high-pressure test data for UHPC, the core parameters were calibrated with reference to the existing literature. Wu (2019) studied the static mechanical properties of UHPC under triaxial stress states and provided the baseline data for parameter calibration. Song et al. (2023) determined and applied the constitutive model parameters for UHPC, and Du et al. (2025) investigated the strain-rate effect of three dynamic constitutive models for UHPC, supporting the rate-related parameter determination. Specifically, the baseline physical property parameters were obtained from fundamental material tests of UHPC. The tensile strain-rate exponent β_t and compressive strain-rate exponent β_c were determined with reference to the research findings reported by Du et al. (2025) and the recommended values given by Borrvall and Riedel (2011). The remaining parameters were adopted from the original values proposed for conventional concrete by Riedel et al. (1999), together with the UHPC-related parameter values reported by Du et al. (2025). The complete set of parameters for the RHT constitutive model is summarized in Table 2.

The K&C constitutive model involves a large number of parameters and requires user-defined strain-rate curves. Although LS-DYNA can automatically generate K&C model parameters based on the uniaxial compressive strength, extensive trial calculations demonstrate that the automatically assigned parameters fail to precisely characterize the mechanical performance of UHPC. Therefore, a complete set of parameter calibrations must be re-executed. The baseline mechanical parameters of the model remain identical to those of the HJC constitutive model. The three sets of limit surface parameters $(a_{ij}\ (i=0,1,2), a_i\ (i=1,2),\ a_{if}\ (i=0,1,2))$ are obtained via curve fitting. The damage parameters$(b_1、\ b_2)$, which respectively govern the compressive and tensile ductility of the material, are

determined through trial-and-error parameter adjustments in uniaxial loading simulations. The parameter controlling volume damage (b_3) directly adopts the values automatically generated by the software. The damage function adjusts the $\lambda - \eta$ relationship curve to ensure that the material's damage evolution trajectory matches the profile of the uniaxial compression test curve, where η is divided into two transitional intervals of 0-1 and 1-0. The strain-rate curves and the damage function are established with reference to the literature. The strain-rate effects of UHPC in tension were reviewed by Thomas and Sorensen (2017) and experimentally characterized by Hu et al. (2018). The strain-rate effect of dynamic constitutive models for UHPC was investigated by Du et al. (2025), and an improved calibration method of the K&C model was proposed by Lee et al. (2021). The remaining parameters adopt the empirical values reported by Riedel et al. (1999) for conventional concrete and by Du et al. (2025) for UHPC. The parameters of the K&C constitutive model are summarized in Table 3.

Table 2 Summary of mechanical parameters for the RHT concrete constitutive model

Limit surface parameters		Damage parameters		Equation of state parameters		Basic material parameters		Other parameters	
A	0.2328	$\varepsilon_p{}^m$	0.0018	T_1	35.27GPa	F_c	111.3MPa	ζ	0.95
N	1.3			T_2	0	G	20.37GPa	β_t	0.005
A_f	2.0488	D_1	0.04	B_0	1.22	ρ	2.54 g·cm-3	β_c	0.005
N_f	0.49			B_1	1.22	α_0	1.0487	g_c^*	0.53
Q_0	0.6805	D_2	1.0	A_1	35.27GPa	n_p	3.0	g_t^*	0.7
B	0.0105			A_2	39.58GPa	f_t^*	0.0678		
				A_3	9.04GPa	f_s^*	0.1		

Table 3 Summary of mechanical parameters for the K&C concrete constitutive model

Limit surface parameters						Damage parameters		Basic material parameters	
a_0	0.236	$a_{0\gamma}$	0.023	a_{1f}	0.344	b_1	0.35	ρ	2.54 g cm^{-3}
a_1	0.344	$a_{1\gamma}$	0.344	a_{2f}	1.444	b_2	-5.80	Fc	111.3 MPa
a_2	2.211	$a_{2\gamma}$	3.109			b_3	1.15	ν	0.227

When only the compressive strength of UHPC is inputted, the K&C model automatically generates the parameters for Equation of State (EOS) No. 8 in LS-DYNA. However, regarding EOS No. 8, which governs the high-pressure volumetric compression characteristics of the material, the initial parameters automatically generated by the software fail to precisely characterize the elastoplastic features of UHPC. Consequently, the modified EOS parameters adopted in this study are determined with reference to the existing literature (Du et al. 2025), and their specific values are summarized in Table 4. In the corresponding formulations, $\ln(V/V_0)$ represents the volumetric strain (volumetric change), *P* denotes the hydrostatic pressure, and K_0 is the unloading bulk modulus.

Table 4 Summary of modified parameters for EOS No. 8 accompanying the K&C model

Ln(V/V$_0$)	P/MPa	K/GPa
0	0	28.23
-0.0015	42.34	28.23
-0.0043	92.30	28.62
-0.0101	171.38	34.76
-0.0305	325.62	41.36
-0.0513	491.11	47.99
-0.0726	696.76	54.58
-0.0943	1065.96	59.57
-0.174	6223.41	134.03
-0.208	9518.73	163.22

3.2 Finite Element Mesh Convergence Analysis

Mesh convergence analysis is systematically conducted for the UHPC target using five grid sizes (1.6, 1.4, 1.2, 1.1, and 1.0 mm) within the core penetration zone. The final depth of penetration (DOP) is selected as the quantitative evaluation metric to characterize the model's convergence behavior.

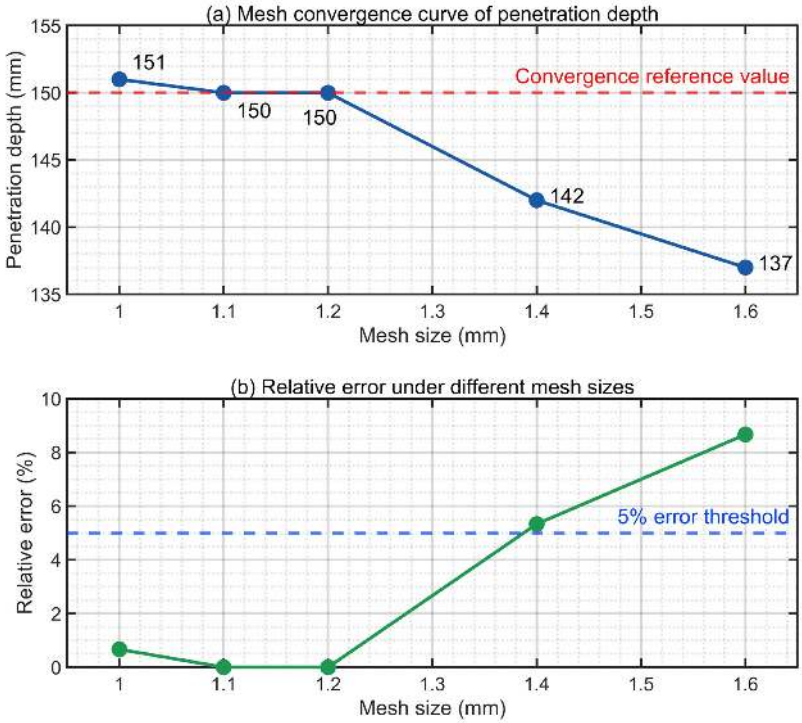

Figure 5: Results of mesh convergence analysis: (a) Mesh convergence curve of penetration depth; (b) Relative error under different mesh sizes.

Figure 5 illustrates the mesh sensitivity analysis for the DOP and relative errors. As shown in Figure 5(a), refining the mesh size from 1.6 mm to 1.2 mm causes the DOP to rise from 137 mm to 150 mm, after which it plateaus at 150–151 mm for grid sizes of 1.1 mm and 1.0 mm. Taking the 1.1 mm mesh as the reference solution (Figure 5(b)), the coarse 1.4 mm and 1.6 mm meshes yield relative errors of 5.33% and 8.67%, respectively, both exceeding the 5.0% accuracy threshold. Conversely, the 1.2 mm mesh satisfies the convergence criterion. Since further refinement to 1.0 mm offers negligible accuracy gains but drastically elevates computational overhead, a mesh size of 1.1 mm is selected for the target region.

3.3 Numerical Model for High-Velocity Projectile Penetration into UHPC

In the aforementioned finite element (FE) model for the numerical simulations, the dimensions of both the projectile and the UHPC target are consistent with those reported in the literature (Lü et al. 2022). Both components are discretized using 3D solid elements with the default constant stress solid element formulation (ELFORM = 1). To prevent rigid-body translation, boundary conditions are enforced by fully constraining a node set defined along the circumference of the target plate. The impact velocity of the projectile is prescribed via the keyword *INITIAL_VELOCITY_GENERATION. The interaction and material erosion at the projectile-target interface are governed by the *CONTACT_ERODING_SURFACE_TO_SURFACE algorithm.

The projectile is characterized using the rigid material model (*MAT_RIGID), with its specific mechanical parameters summarized in Table 5. To support the rigid-projectile assumption, the corresponding Johnson-Cook constitutive parameters of the 30CrMnSiNi2A high-strength alloy steel are additionally summarized in Table 6, whose sufficiently high yield and ultimate strengths ensure negligible plastic deformation during penetration. The UHPC target is modeled using the HJC, RHT, and K&C constitutive models, respectively, and their corresponding calibrated parameters are provided in the previously established Tables 1–4. Based on the mesh convergence results, a mesh size of 1.1 mm is adopted for the UHPC target region. To optimize computational efficiency, a half-symmetric (1/2) model configuration is utilized, and the assembled projectile-target numerical model is illustrated in Figure 6.

Table 5 Material parameters of the rigid projectile (MAT_RIGID)

ρ (g/cm3)	E (/GPa)	υ
7.8	210	0.3

Note: $\boldsymbol{\rho}$ is density, E is elastic modulus,$\boldsymbol{\nu}$ is Poisson's ratio.

Table 6 The Johnson-Cook model parameters of 30CrMnSiNi2A Steel

ρ (g/cm3)	G (/GPa)	A (/MPa)	B(/MPa)	n_p	C	D_1	D_2	D_3	D_4
7.8	81	1269	810	0.479	0.04	0.239	8.593	7.867	0.009

Note: G is shear modulus, A is yield strength, B and n_p are strain-hardening coefficients, C is strain-rate sensitivity coefficient, D_1-D_4 are damage parameters.

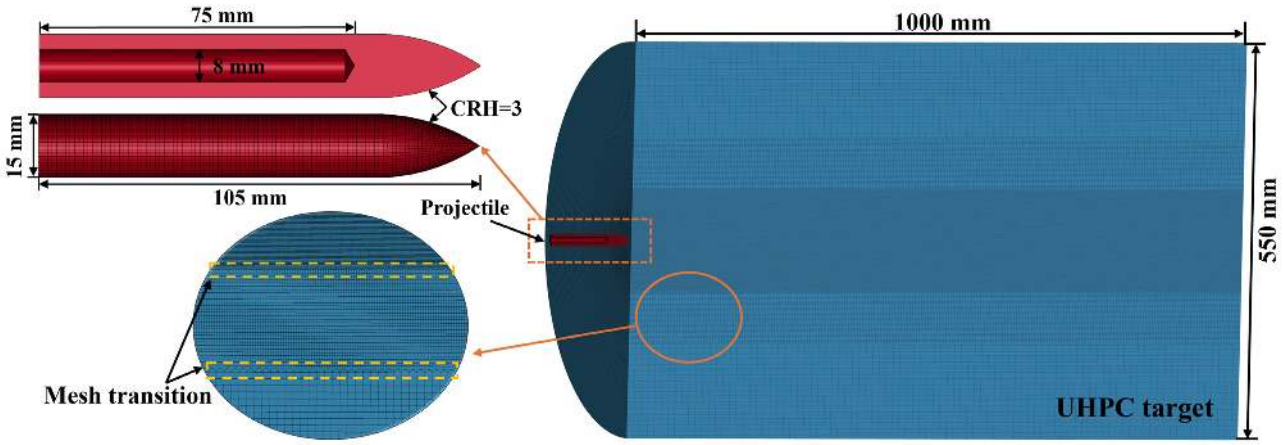

Figure 6: Finite element model for projectile impact on UHPC

To characterize the material failure behavior, element erosion of the UHPC target is governed by the keyword *MAT_ADD_EROSION. Reasonable erosion parameters were obtained in this study through repeated numerical trials and comparisons with experimental results, in which the thresholds of maximum effective strain (EFFEPS) and volumetric strain (VOLEPS) were set to 1.2 and 0.2, respectively. In addition, the keyword *CONTROL_HOURGLASS was adopted to suppress non-physical hourglass energy.

3.4 Benchmarking Analysis of Simulation Responses against Experimental Data for the Three Constitutive Models

To validate the calibrated HJC, RHT, and K&C parameters for C120 UHPC, numerical simulations are benchmarked against the ballistic tests by Lü et al. (2022). The experiments involve a 30CrMnSiNi2A hard steel projectile penetrating a thick UHPC target at striking velocities of 633, 728, and 959 m/s, yielding measured depths of penetration (DOP) of 136, 177, and 262 mm, respectively. Maintaining strictly identical mesh sizes (1.1 mm), boundary conditions, and erosion criteria, the simulated DOPs for each model are compared with the experimental data in Table 7.

Table 7 Comparison of simulated and experimental DOPs for the three constitutive models

Impact velocity (m/s)	Experimental DOP (mm)	HJC simulated DOP (mm)	HJC relative error (%)	RHT simulated DOP (mm)	RHT relative error (%)	K&C simulated DOP (mm)	K&C relative error (%)
633	136	122	-10.29	122	-10.29	149	+9.56
728	177	151	-14.69	142	-19.77	168	-5.08
959	262	234	-10.69	205	-21.76	193	-26.34

(**Note:** Relative error =[(Simulated value − Measured value)/Measured value] × 100%)

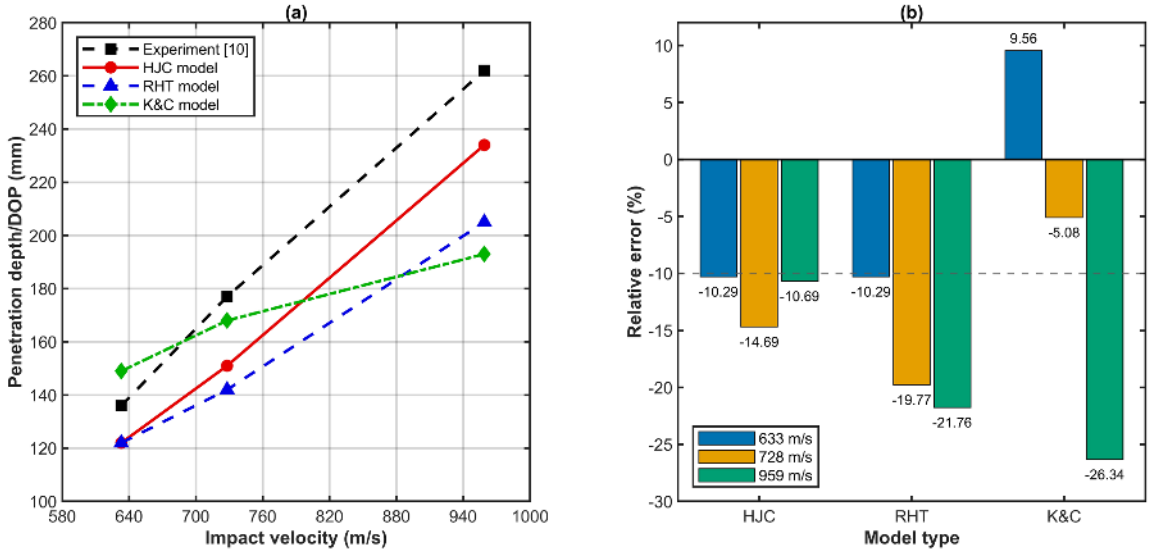

Figure 7: Comparison of simulated DOP and relative error distributions for the three constitutive models: (a) evolution curves of DOP versus velocity; (b) grouped bar chart of relative error distribution. (Experimental data from Lü et al. 2022)

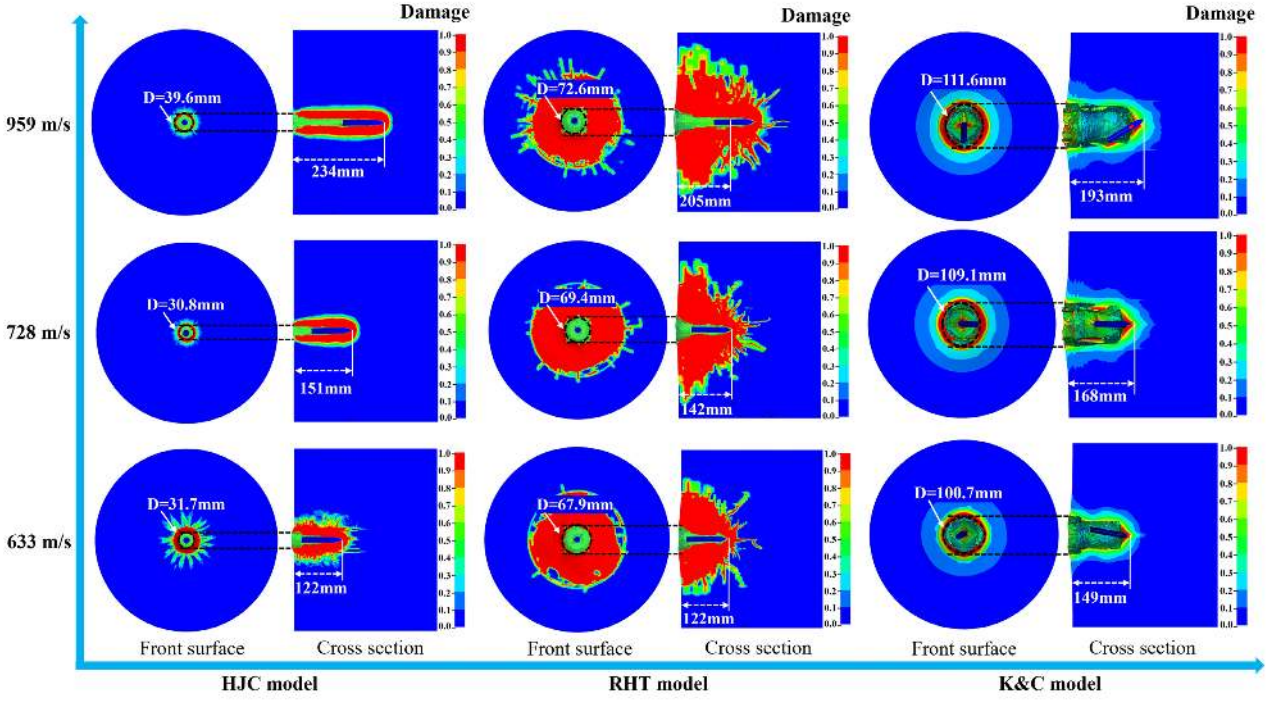

Figure 8: Comparison of target surface crater morphology and cross-sectional damage for the three constitutive models at striking velocities of 633, 728, and 959 m/s

Table 7 and Figure 7 and Figure 8 reveal that the three models exhibit pronounced divergence in resistance feedback and energy dissipation under high-velocity impact:

HJC Model: The HJC model exhibits superior stability, maintaining a consistent DOP underestimation (errors within -10% to -15%) that mirrors experimental trends well. Its damage contours reveal a highly localized penetration tunnel with minimal surface cratering (30.8-39.6 mm) and no lateral shear collapse. This localized topology successfully captures the intense shear confinement and fiber-bridging effects of the dense UHPC matrix, which effectively channels the projectile's kinetic energy into axial cavity expansion.

RHT Model: The RHT model significantly underestimates the target resistance at high velocities. While its prediction at 633 m/s matches the HJC model, its predicted DOPs at 728 and 959 m/s (142 mm and 205 mm) deviate severely, with relative errors expanding to -19.77% and -21.76%. It exhibits a non-localized spallation mode characterized by large surface craters and extensive cross-sectional radial cracks forming a wide funnel-shaped damage zone. This discrepancy occurs because the piecewise limit surfaces and dynamic volumetric compression formulation of the RHT model fail to capture the mechanical response of UHPC under high hydrostatic pressures, leading to accelerated damage evolution and premature strength softening.

K&C Model: The K&C model shows a pronounced polarization in prediction accuracy with varying striking velocities. It yields good agreement at low-to-moderate speeds, but its prediction drops precipitously to 193 mm (relative error of -26.34%) at 959 m/s. The damage contours present extensive lateral plastic dissipation (100.7-111.6 mm). This is attributed to the radial scaling mechanism of the K&C model, which induces excessive enhancement of the lateral strength under high-rate and high-pressure loading. Consequently, a massive amount of impact energy is misdirected into lateral squeezing, causing projectile trajectory deviation and a failure to replicate the hydrodynamic response of cavity expansion.

In summary, the calibrated HJC constitutive model is selected as the core framework for the numerical simulations in this study. The model achieves a stable average relative error of -11.89% for the DOP without high-speed divergence. Its localized straight trajectory and small surface crater match the high toughness and fiber-bridging effects of UHPC, successfully avoiding the inherent deficiencies of the RHT and K&C models. This validation establishes a reliable numerical foundation for subsequent investigations into penetration mechanisms. From a practical perspective, the superiority of the HJC model provides a model-selection reference for the impact-resistant design of UHPC protective structures, reducing the uncertainty caused by RHT over-softening and K&C crater overestimation. This recommendation aligns with previous studies on UHPC penetration: the state-of-the-art review by Liu et al. (2022) emphasized the dominant role of strain-rate effects in the high-velocity impact response of UHPC, and Song et al. (2023) successfully applied the HJC parameters to UHPC impact simulations.

4 Modified Model for High-Velocity Penetration into Homogeneous UHPC

To ensure consistency in simulation configurations and boundary conditions, this section retains the calibrated HJC constitutive parameters, erosion control algorithms, and the 1.1-mm mesh discretization scheme within the core ballistic zone. The striking velocity of the projectile is prescribed across a range of 800-1500 m/s, encompassing eight typical high-velocity conditions, to systematically investigate the dynamic responses and extended penetration mechanisms of rigid projectiles into UHPC.

4.1 Analysis of High-Velocity Penetration Response and Damage Evolution in UHPC

4.1.1 Evolution of Simulated Depth of Penetration (DOP) under High-Velocity Conditions

Based on the numerical simulations, Figure 9 illustrates the depths of penetration (DOP) of the rigid projectile and their evolution trends across a striking velocity range of 800-1500 m/s. The corresponding quantitative data are summarized in Table 8.

Numerical results within the 800-1500 m/s range reveal a non-linear accelerated growth trend for the DOP. The DOP increment escalates from 38-40 mm per 100 m/s at moderate velocities (800-1000 m/s) to 55-56 mm per 100 m/s in the ultra-high-velocity hydrodynamic regime (>1200 m/s).

This trend is governed by the rigid projectile assumption, which eliminates deformation and mass erosion to keep the ogival nose completely intact. Although ultra-high-velocity impact generates hydrodynamic inertial resistance proportional to v^2, the absence of mass stripping prevents rapid kinetic energy decay. Consequently, the stable nose geometry maintains continuous contact pressure to overcome target cavity expansion resistance, driving steady DOP growth.

4.1.2 Penetration Tunnel Morphology and Localized Damage Mechanisms

Analysis of the cross-sectional damage contours under the eight velocity conditions (Figure 10) elucidates the damage evolution and intrinsic energy dissipation mechanisms of the UHPC target under the homogeneous material assumption.

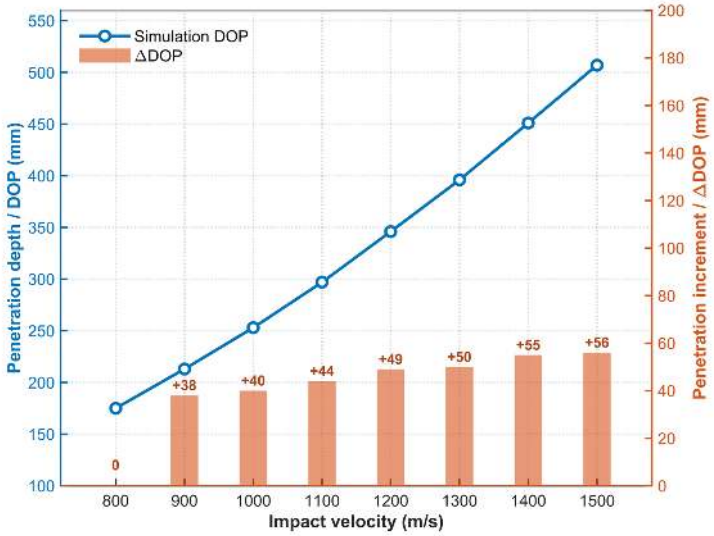

Figure 9: Simulated depth of penetration (DOP) and corresponding DOP increments at striking velocities of 800-1500 m/s

Table 8 Simulated depths of penetration at striking velocities of 800-1500 m/s

Impact velocity (m/s)	Simulated DOP (mm)	DOP increment (mm)
800	175	—
900	213	+38
1000	253	+40
1100	297	+44
1200	346	+49
1300	396	+50
1400	451	+55
1500	507	+56

Penetration Trajectory and Confinement: As the striking velocity escalates from 800 to 1500 m/s, the DOP increases from 175 to 507 mm. Throughout this velocity range, the penetration trajectory consistently maintains a rectilinear tunnel morphology with intact walls and no discernible lateral shear spallation or large-scale collapse. This damage morphology indicates that the dense matrix provides exceptional lateral confinement pressure, effectively suppressing the radial dispersion of impact energy. Consequently, most kinetic energy is confined within the axial cavity expansion zone ahead of the projectile nose, driving the longitudinal extension of the penetration tunnel.

Mechanism Mapping Effect: Notably, although the target is simplified as a homogeneous continuum without discrete steel fibers in the numerical model, the simulated highly localized shear damage features macroscopically mirror the crack-bridging and energy dissipation effects induced by steel fibers in actual UHPC. Under the coupled loading of high pressures and high strain rates from cavity expansion waves, the lateral stiffness confinement generated by the homogeneous medium replicates the mechanical effect of dynamic fiber pull-out energy dissipation at tension-shear microcracks. This effect effectively suppresses the propagation of secondary cracks around the penetration tunnel, preserving the dynamic integrity of the target structure.

4.2 Formulation and Parameter Calibration of the Modified Theoretical Model

4.2.1 Limitations of Classical Cavity Expansion Theory and Deficiencies in High-Velocity Penetration Prediction

To quantitatively characterize the deceleration behavior and energy dissipation mechanisms of the rigid projectile during the stable deep penetration phase, the Forrestal resistance model (Forrestal et al. 1997), formulated based on the dynamic cavity expansion theory, is adopted in this section. When an ideal rigid ogival projectile undergoes deep axial penetration into a semi-infinite UHPC target, its one-dimensional non-linear governing equation of motion can be expressed via Newton's second law as:

$$M\frac{dv}{dt} = -F_z \tag{9}$$

where: *M* denotes the physical mass of the rigid projectile; *v* is the instantaneous velocity of the projectile; F_z represents the transient total axial resistance exerted by the target on the projectile head during penetration. In the steady tunneling penetration stage, the total axial resistance F_z acting on the ogival projectile head from the target can be decomposed into two components: a static resistance term and a fluid inertial term.

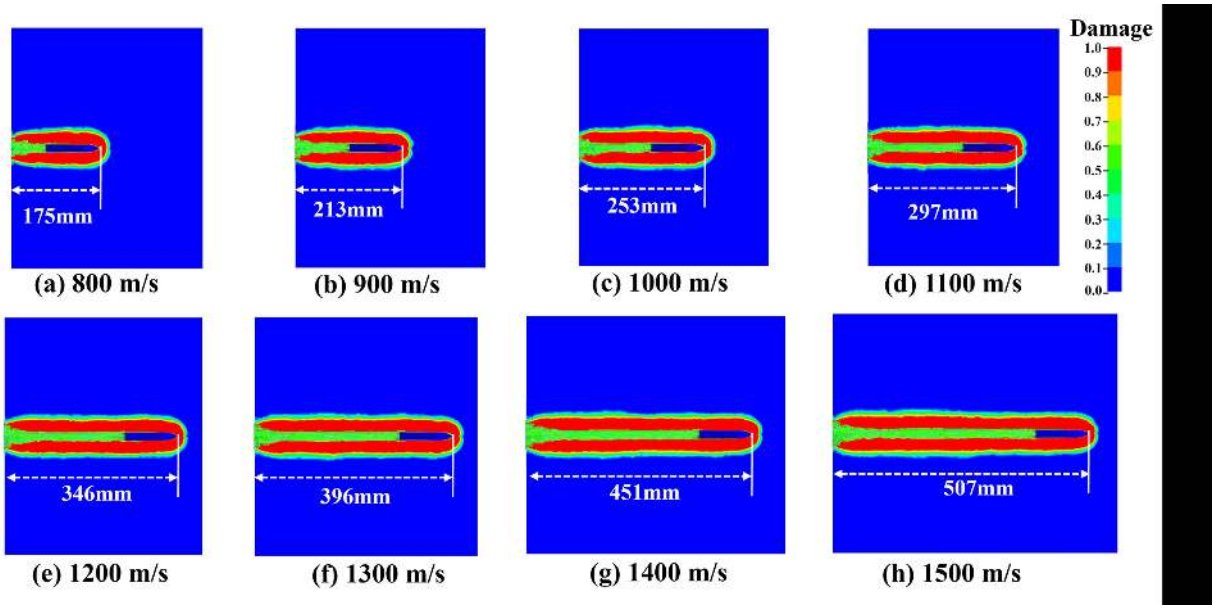

Figure 10: Cross-sectional damage contours of the target plate under high-velocity penetration at striking velocities of 800-1500 m/s

$$F_z = \pi R^2 (S_0 f_c + N\rho_t v^2) \tag{10}$$

Where: *R* = projectile radius; f_c = quasi-static compressive strength of target material; ρ_t= target density; *N* = projectile nose geometric factor; S_0= initial dimensionless static confining constraint coefficient. The time variable is eliminated via the chain rule for composite functions to satisfy transformation relations. Spatial initial boundary conditions are defined for tunneling penetration: the instantaneous velocity equals the initial impact velocity V_0 at displacement $x = 0$, and the projectile velocity drops to $v = 0$ at the maximum penetration depth $x = X_t$, as expressed in the following formula:

$$\int_0^{X_t} \mathrm{d}x = \int_{V_0}^{0} \frac{Mv}{-\pi R^2 \left(S_0 f_c + N\rho_t v^2\right)} \mathrm{d}v \tag{11}$$

$$X_t = \int_0^{V_0} \frac{Mv}{\pi R^2 (S_0 f_c + N\rho_t v^2)} \mathrm{d}v = \frac{2M}{\pi d^2 N\rho_t} \ln\left(1 + \frac{N\rho_t V_0^2}{S_0 f_c}\right) \tag{12}$$

Mathematically, the classical formula yields a logarithmic relationship between the depth of penetration (DOP) and striking velocity. Its first derivative $(\mathrm{d}X_t/\mathrm{d}V_0)$ monotonically decreases, exposing a pronounced velocity saturation effect. This trend contradicts the simulation results in Table 8, where the DOP increments continuously rise under ultra-high-velocity impact, exhibiting non-logarithmic accelerated growth. Consequently, the assumption of a constant strength parameter fails to capture the dynamic resistance evolution of UHPC at ultra-high velocities, necessitating a modification to the analytical framework.

To remedy these deficiencies, two key modifications are introduced below. The first is a dynamic strengthening coefficient that quantifies the strain-rate- and pressure-induced yield enhancement of UHPC at ultra-high velocities. The second is a rheological softening factor that accounts for the shear-thinning fluidization of the comminuted matrix under severe multiaxial confinement. Their mechanical mechanisms are elaborated in the following subsections.

4.2.2 Mechanical Mechanisms of Dynamic Yield Enhancement and Shear Rheological Softening

To address the prediction deviations of classical theoretical models under ultra-high-velocity conditions, a dynamic yield enhancement mechanism for UHPC targets is formulated. HJC simulations indicate that within the 800-1500 m/s range, extreme hydrostatic pressure and ultra-high strain rates trigger a step-like escalation in the dynamic yield stress at the elastoplastic interface, far exceeding the quasi-static strength. Because this intense shock-hardening renders conventional low-velocity resistance constants inapplicable, a dynamic baseline enhancement coefficient is introduced to quantitatively characterize the high-velocity strength hardening of UHPC.

As revealed by the cross-sectional damage evolution in Figure 10, the UHPC matrix within the core high-overload zone of the penetration tunnel is completely crushed (with the damage variable approaching 1.0). Under multiaxial severe confinement, the pulverized matrix exhibits distinct shear fluidization characteristics; its transient shear resistance no longer remains constant but rather demonstrates typical non-linear shear thinning behavior as the shear rate escalates.

4.2.3 Formulation of the Modified Analytical Model for Depth of Penetration (DOP)

Based on Forrestal's classical segmented resistance model of "crater region-tunnel region," the constant confinement coefficient S_0 in the steady-state penetration stage of the traditional model is improved to a composite correction coefficient that incorporates a dynamic baseline strengthening coefficient γ_0 and a high-pressure shear rheological softening factor $\Gamma(V_0)$. Given that the kinetic energy attenuation of the projectile during the cratering stage under high-velocity penetration conditions is negligible, the initial impact velocity V_0 is directly adopted as the integral velocity boundary for the deep tunnel penetration stage. Accordingly, a modified analytical penetration model governing a rigid projectile penetrating a homogeneous UHPC target is established as follows:

$$X = k \cdot d + \frac{2M}{\pi d^2 N \rho_t} \ln\left[1 + \frac{N \rho_t V_0^2}{\gamma_0 S_0 f_c \cdot \Gamma(V_0)}\right] \tag{13}$$

Where *X* is the final penetration depth; M is the physical mass of the rigid projectile, $M = 102$ g; d is the projectile diameter; N is the projectile nose geometry factor, $N = 0.1065$; S_0 is the quasi-static elastic confining-pressure constraint coefficient, $S_0 = 3.85$.

Where the mathematical formulation of the high-pressure shear rheological softening factor $\Gamma(V_0)$ is defined as:

$$\Gamma(V_0) = 1 - \xi\left(\frac{V_0}{C_0}\right)^2 \tag{14}$$

Where C_0 is the intrinsic bulk longitudinal wave velocity of the UHPC matrix ($C_0 = 4200$ m/s); ξ is a dimensionless structural constant that characterizes the velocity-thinning sensitivity induced by high-pressure shear rheology. By introducing a rate-dependent term into the denominator, the model algebraically counteracts the negative feedback from the fluid inertial resistance $N\rho_r V_0^2$ in the numerator. In this way, it mathematically reveals the physical essence that, under high-speed advancement of an ideal rigid projectile, the ultimate penetration-depth curve breaks away from the classical logarithmic saturation constraint and exhibits an accelerated penetration characteristic.

4.2.4 Parameter Calibration via Two-Stage Decoupled Identification

The cratering constants (α, β) are linearly calibrated. The dimensionless crater-depth coefficient *k*, accounting for the brittle shear failure of the homogeneous high-strength matrix at the surface, is expressed as a linear function of the velocity normalized by the matrix bulk sound speed: $k = \alpha \cdot \left(\frac{V_0}{C_0}\right) + \beta$, where α and β are the dimensionless surface cratering constants. A linear least-squares fit to the eight sets of normalized velocities and corresponding *k* values (shown in Fig. 11) yields $\alpha = 3.1817$, $\beta = 1.3570$, with a coefficient of determination $R^2 = 0.9508$.

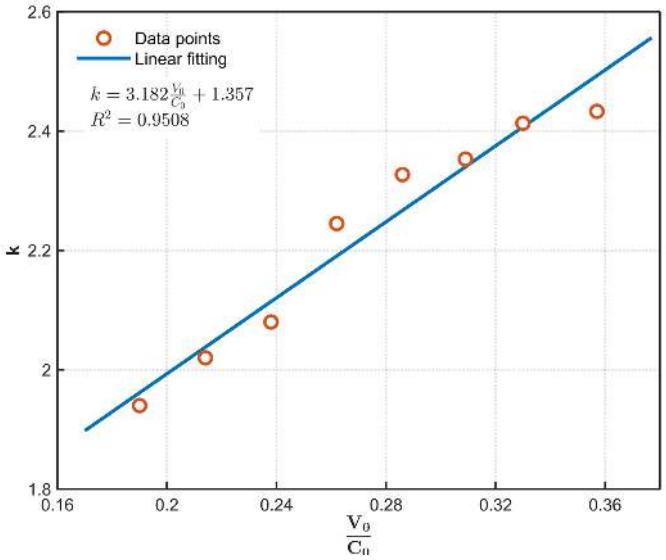

Figure 11: Fitting and calibration of the surface cratering constants α and β against the numerical crater-depth coefficient

Calibration of tunnel-stage dynamic baseline and rheological sensitivity parameters (γ_0, ξ): The quasi-static confining pressure coefficient $S_0 = 3.85$ is kept constant, and the tunnel-stage dynamic baseline and rheological sensitivity parameters γ_0 and ξ are inversely calibrated by fitting to numerical depth-of-penetration (DOP) data obtained for eight impact velocities ranging from 800 to $1500\ \mathrm{m/s}$, using a nonlinear multi-dimensional global optimisation algorithm, which yields $\gamma_0 = 2.8142$ and $\xi = 0.7987$ (as shown in Figure 12).

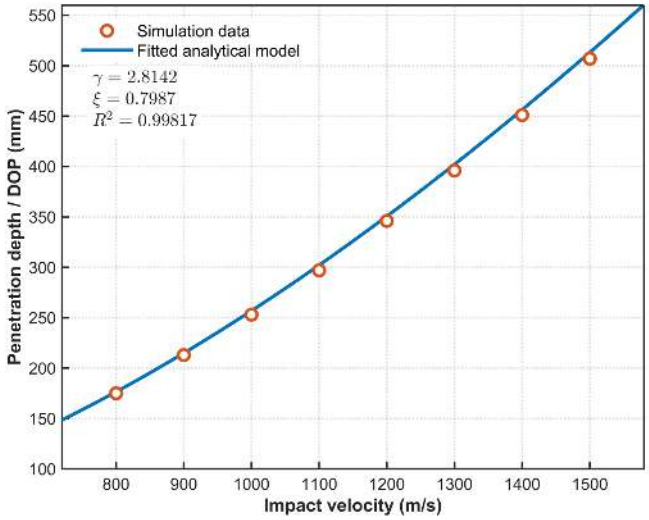

Figure 12: Fitting and calibration of the tunnel-stage parameters γ_0 and ξ using numerical DOP data at 800-1500 m/s

4.3 Accuracy Validation of the Modified Model

To evaluate the predictive accuracy of the proposed modified analytical model, the theoretical calculation results are compared against the measured ballistic experimental data of rigid projectiles penetrating UHPC targets (Lü et al. 2022). It should be noted that the present validation is confined to the UHPC material, the projectile configuration, and the velocity range covered by these experiments; validation under different materials and impact conditions is required to further extend the applicability of the model (see Section 5). As illustrated in Figure 13, the theoretical prediction curve of the modified model is benchmarked against the experimental data points spanning from the low- to ultra-high-velocity regimes. Quantitative error metrics indicate that the maximum relative error between the theoretical predictions and experimental values across the entire velocity domain is merely 14.54%, with the overall error strictly constrained within 15%. Furthermore, the model demonstrates satisfactory predictive convergence characteristics under high-velocity conditions.

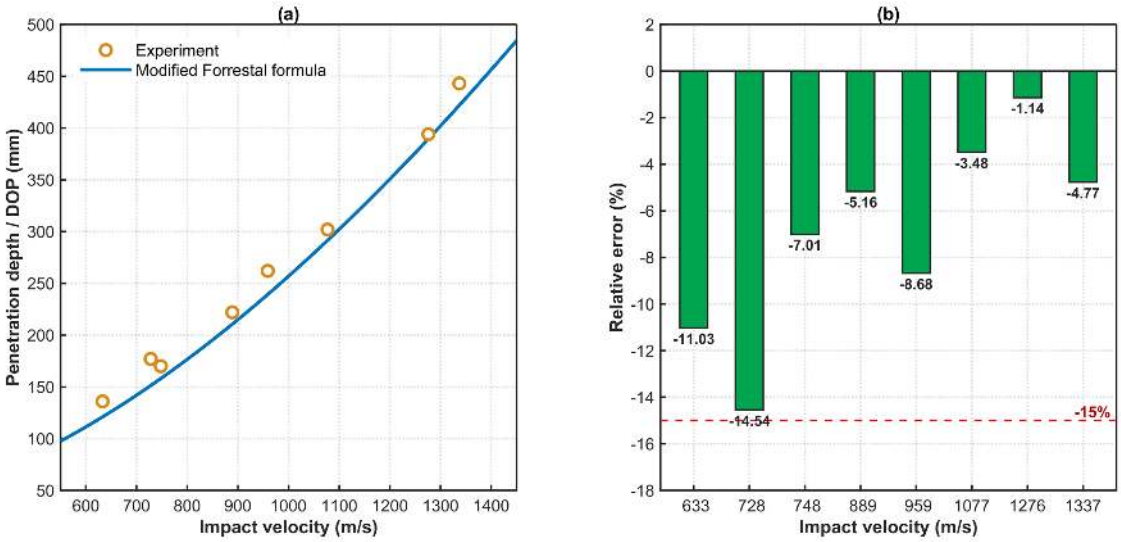

Figure 13: Comparison between the modified model and experimental data: (a) comparison of theoretical and experimental DOP for the modified model; (b) relative error of theoretical DOP against experimental results (Experimental data from Lü et al. 2022)

In summary, within the material and impact conditions covered by the experiments (a C120 UHPC target penetrated by a rigid projectile in the 633–1337 m/s range), the proposed modified analytical model captures the evolution of the final depth of penetration (DOP) with good accuracy and a physically sound mechanism. By mitigating the prediction deviations inherent in classical frameworks within the ultra-high-velocity regime, the model enables quantitative evaluation of DOP in the validated velocity range. Consequently, under these conditions, this work provides a preliminary theoretical basis for the impact-resistant design and ballistic performance evaluation of UHPC protective structures; extension to other materials and conditions requires further validation as discussed in Section 5. From an engineering viewpoint, the modified analytical model serves as a rapid evaluation tool for the preliminary design of UHPC protective structures under ultra-high-velocity threats, requiring only the basic material properties and the projectile-target geometry. The revealed dynamic strengthening and rheological softening mechanisms also provide guidance for material-level design. The predicted DOPs agree well with the ballistic measurements of Lü et al. (2022), and the correction of the classical Forrestal cavity-expansion model is consistent with the systematic underestimation of penetration resistance reported in previous analytical studies on UHPC.

5 Conclusions

Based on the systematic numerical evaluation of constitutive models and the development of a modified analytical framework for rigid projectiles penetrating UHPC targets at 800-1500 m/s, the primary conclusions are drawn as follows:

1. Constitutive Model Evaluation and Selection: Among the evaluated models, the calibrated HJC model demonstrates the highest accuracy and stability within the 633-959 m/s range, yielding a stable DOP error (average -11.89%) and capturing realistic damage morphologies without divergence. Conversely, the RHT model underpredicts penetration depth (error expanding to -21.76%) due to premature high-pressure shear softening. The K&C model exhibits severe accuracy polarization, with its error sharply escalating to -26.34% at 959 m/s because its radial scaling mechanism artificially overestimates lateral strength. Therefore, the HJC model is recommended as the preferred framework for high-velocity UHPC penetration simulations.

2. Penetration Resistance Evolution and Mechanical Mechanisms: Within the 800-1500 m/s range, the final DOP exhibits a pronounced non-linear accelerated growth with striking velocity, directly contradicting the logarithmic deceleration trend predicted by classical Forrestal theory. This accelerated penetration behavior is governed by a competitive two-fold mechanism: the extreme hydrostatic pressure ahead of the projectile nose activates dynamic yield enhancement to boost local resistance, whereas the pulverized medium within the tunneling zone undergoes shear fluidization. The latter manifests as a non-linear rheological softening behavior where the equivalent target resistance decreases as the local shear rate escalates.

3. Formulation and Validation of the Modified Analytical Model: A modified analytical model for rigid projectiles penetrating UHPC targets is established by integrating dynamic strength enhancement and shear rheological softening factors into the Forrestal framework. Validated against ballistic experiments across 633-1337 m/s, the model constrains the relative error within 15% (with a maximum error of 14.54%). This framework effectively eliminates the systemic underestimation of the DOP inherent in classical cavity expansion theory, demonstrating good predictive capability within the validated velocity range.
4. Limitations and Future Work: The present validation is confined to a single UHPC mixture (C120) and one rigid-projectile configuration under axisymmetric normal penetration, and the projectile deformation was not considered. Broader validation with additional mixtures, projectile geometries, and oblique impacts, as well as the adoption of a deformable projectile model, is recommended in future work.

Author's Contributions: Yalong Wang, Wenbin Li; Methodology, Yalong Wang; Software, Yalong Wang, Yiming Li; Investigation, Yalong Wang; Data curation, Yalong Wang, Guixiang Yin, Zhongqiang Cheng; Visualization, Yalong Wang, Zhongqiang Cheng, Yiming Li; Writing - original draft, Yalong Wang; Writing - review & editing, Wenbin Li; Supervision, Wenbin Li; Resources, Wenbin Li; Funding acquisition, Wenbin Li; Project administration, Wenbin Li; Result analysis, Guixiang Yin; Literature sorting, Kun Zhang; Formal analysis, Kun Zhang; Validation, Ronghua Ma; Manuscript polishing, Ronghua Ma.

Data Availability statement: Research data is only available upon request.

Editor: Marcilio Alves.

References

Liu, J., Li, J., Fang, J., Su, Y., Wu, C. (2022). Ultra-high performance concrete targets against high velocity projectile impact – a state-of-the-art review. International Journal of Impact Engineering 160:104080.

Yu, R., Spiesz, P., Brouwers, H.J.H. (2016). Energy absorption capacity of a sustainable Ultra-High Performance Fibre Reinforced Concrete (UHPFRC) in quasi-static mode and under high velocity projectile impact. Cement and Concrete Composites 68:109–122.

Lai, J.Z., Guo, X.J., Zhu, Y.Y. (2014). Properties of ultra-high performance concrete subjected to penetration and explosion. Journal of Hebei University of Technology 43(6):50–54.

Bragov, A.M., Petrov, Y.V., Karihaloo, B.L., et al. (2013). Dynamic strengths and toughness of an ultra high performance fibre reinforced concrete. Engineering Fracture Mechanics 110:477–488.

Hu, L., Li, Y.C., Tang, Z.Q., Yang, S.L. (2023). Experimental study on dynamic performance of UHPC based on SHPB. Protective Engineering 45 (05):13-21.

Yang, W., Xie, Y.H., Bi, Y., Luo, Y.L., Yan, X.Y., Gao, Y.X. (2022). Influence of steel fiber volume content and types on tensile stress–strain of ultra-high performance concrete. Concrete (5):37–46.

Du, X.L., Tian, Y.D., Tian, R.J., Zhang, L. (2009). Mechanical property test of steel fiber ultra-high strength concrete. Journal of Beijing University of Technology 35(9):1198–1203.

Han, J.C., Lyu, L.M., Hu, L., Gao, Z., Wang, R.L., Chen, Y.Q. (2024). Dynamic fracture mechanisms and mechanical property enhancement effects in UHPFRC. Protective Engineering 46(6):9-17.

Liu, B.L. (2023). Effect of hybrid fibers on dynamic mechanical properties of UHPC. Master's thesis, Southwest University of Science and Technology, China.

Li, M.Z., Mao, J.Z., Li, L., Wang, J.L., Meng, L.Q., Zhang, C.X. (2024). Dynamic compressive properties of UHPC under one-dimensional stress wave: The influence of steel fiber morphology and curing regime. Journal of Building Engineering 89:109382.

Yu, Q.L., Zhuang, W.T., Shi, C.J. (2021). Research progress on the dynamic compressive properties of ultra-high performance concrete under high strain rates. Cement and Concrete Composites 124:104258.

Dong, H.W., Li, Y., Jin, A.G., Yang, H., Chen, J.Y. (2026). Mechanical-electric response characteristics of 2–2 UHPC based piezoelectric composite under impact loading. Mechanics Research Communications 151:104579.

Guo, W., Fan, W., Shao, X.D., Shen, D.J., Chen, B.S. (2018). Constitutive model of ultra-high-performance fiber-reinforced concrete for low-velocity impact simulations. Composite Structures 185:307–326.

Zhou, F., Su, Q., Cheng, Y.H., Wu, H. (2023). A novel dynamic constitutive model for UHPC under projectile impact. Engineering Structures 280:115711.

Das, N., Nanthagopalan, P. (2024). Ballistic impact resistance of ultra-high-performance concrete (UHPC): A comprehensive experimental investigation and parametric analysis. International Journal of Impact Engineering 187:104912.

Yang, S.B., Kong, X.Z., Wu, H., Fang, Q., Xiang, H.B. (2021). Constitutive modelling of UHPCC material under impact and blast loadings. International Journal of Impact Engineering 153:103860.

Holmquist, T.J., Johnson, G.R., Cook, W.H. (1993). A computational constitutive model for concrete subjected to large strains, high strain rates, and high pressures. Proceedings of the 14th International Symposium on Ballistics, Quebec, Canada, pp. 591–600.

Riedel, W., Thoma, K., Hiermaier, S., Schmolinske, E. (1999). Penetration of Reinforced Concrete by BETA-B-500: Numerical Analysis using a New Macroscopic Concrete Model for Hydrocodes. Proceedings of the Relevant Ballistics Symposium.

Malvar, L.J., Crawford, J.E., Wesevich, J.W., Simons, D. (1997). A plasticity concrete material model for DYNA3D. International Journal of Impact Engineering 19(9–10):847–873.

Pany, C. (2021a). Estimation of correct long-seam mismatch using FEA to compare the measured strain in a non-destructive testing of a pressurant tank: A reverse problem. International Journal of Smart Vehicles and Smart Transportation 4(1):1-13.

Pany, C. (2021b). Cylindrical shell pressure vessel profile variation footprint in strain comparison of test data with numerical analysis. Liquid and Gaseous Energy Resources 1(2):91–101.

Pany, C. (2022). Investigation of circular, elliptical and obround shaped vessels by finite element method (FEM) analysis under internal pressure loading. Journal of Science, Technology and Engineering Research 3(1):24-31.

Sun, Q.R., Li, R.Y., Zhao, Y.Y., Sun, Y.X. (2016). Investigation on parameters of HJC model applied to simulate perforation experiments of reinforced concrete. Engineering Mechanics 33(8):248–256.

Ma, T.B., Wu, J., Ning, J.G. (2019). Experimental and numerical study on projectiles' high-velocity penetration into reinforced concrete. Explosion and Shock Waves 39(10):103301.

Wang, Z.L., Li, Y.C., Shen, R.F., Wang, J.G. (2007). Numerical study on craters and penetration of concrete slab by ogive-nose steel projectile. Computers and Geotechnics 34(1):1–9.

Zou, Y., Jiang, J.L., Yang, J., Zhang, Z.Y., Guo, J.C. (2023). Enhancing the toughness of bonding interface in steel-UHPC composite structure through fiber bridging. Cement and Concrete Composites 137:104947.

Su, Q., Wu, H., Fang, Q. (2022). Calibration of KCC model for UHPC under impact and blast loadings. Cement and Concrete Composites 127:104401.

Wan, W.Z., Yang, J., Xu, G.J., Liu, Y.K. (2021). Determination and evaluation of Holmquist-Johnson-Cook constitutive model parameters for ultra-high-performance concrete with steel fibers. International Journal of Impact Engineering 156:103966.

Song, S., Du, C., Li, Y.Y. (2023). Determination and application of the HJC constitutive model parameters for ultra-high performance concrete. Explosion and Shock Waves 43(5):053102.

Du, C., Song, S., Wang, H.Z., Wu, B.Y., Li, Y.Y. (2025). Research on strain rate effect of three dynamic constitutive models for UHPC. Journal of Dynamic Disasters 1(4):100052.

Yan, L., Chen, L., Chen, B.Y., Fang, Q. (2025). Analysis and evaluation of suitability of high-pressure dynamic constitutive model for concrete under blast and impact loading. International Journal of Impact Engineering 195:105145.

Wang, M.Y., Zheng, D.L., Qian, Q.H. (2004). Scale conversion relationship for projectile penetration and perforation into concrete medium. Explosion and Shock Waves 24(2):108–114.

Wang, D.R., Ge, T., Zhou, Z.P., et al. (2006). Study on anti-penetration calculation method of steel fiber ultra-high strength reactive powder concrete (RPC). Explosion and Shock Waves (4):367–372.

Forrestal, M.J., Tzou, D.Y. (1997). A spherical cavity-expansion penetration model for concrete targets. International Journal of Solids and Structures 34(31–32):4127–4146.

Rong, Z.D., Sun, W., Zhang, Y.S., She, W. (2010). Anti-penetration behavior of ultra-high performance steel fiber reinforced concrete and its numerical simulation. Journal of the Chinese Ceramic Society 38(9):1723–1728.

Pham, T.M., Hyde, H., Kaung, M.K., Zhuge, Y., Tran, D.T., Vlietstra, D., Tran, T.M. (2024). Comparative impact behaviours of ultra high performance concrete columns reinforced with polypropylene vs steel fibres. Defence Technology 40:138–153.

Blasone, M., Saletti, D., Baroth, J., Forquin, P., Bonnet, E., Delaplace, A. (2021). Ultra-high performance fibre-reinforced concrete under impact of an AP projectile: Parameter identification and numerical modelling using the DFHcoh-KST coupled model. International Journal of Impact Engineering 152:103838.

Zhou, F., Yin, S.P., Jiang, X., Xu, S.L. (2024). Prediction method of penetration depth and projectile residual velocity of UHPC based on the uniaxial strain response. Engineering Mechanics.

Fan, H.T., Yu, H.F., Ma, H.Y. (2023). Dynamic increase factor(DIF) of concrete with SHPB tests: Review and systematic analysis. Journal of Building Engineering 79:107666.

Polanco-Loria, M., Hopperstad, O.S., Børvik, T., Berstad, T. (2008). Numerical predictions of ballistic limits for concrete slabs using a modified version of the HJC concrete model. International Journal of Impact Engineering 35:290–303.

Zhou, F., Cheng, Y.H., Peng, Q., Wu, H. (2023). Influence of steel reinforcement on the performance of an RC structure subjected to a high-velocity large-caliber projectile. Structures 54:716–731.

Wang, Z.H., Wen, H.M., Zheng, H., Cheng, J.S. (2022). Dynamic increase factors of concrete-like materials at very high strain rates. Construction and Building Materials 345:128270.

Khan, M.M., Iqbal, M.A. (2024). Strain rate and size effects on dynamic tensile behaviour of standard and high-strength concrete: An experimental study. Structures 63:106325.

Tedesco, J.W., Ross, C.A. (1998). Strain-Rate-Dependent Constitutive Equations for Concrete. Journal of Pressure Vessel Technology 120(4):398–405.

Hassan, M., Wille, K. (2022). Direct tensile behavior of steel fiber reinforced ultra-high performance concrete at high strain rates using modified split Hopkinson tension bar. Composites Part B: Engineering 246:110259.

Li, M.Z., Mao, J.Z., Li, L., Liu, J.B., Liu, F. (2025). Dynamic tensile properties and spall strength of strain hardening ultra-high performance concrete under one-dimensional stress wave. Journal of Building Engineering 108:112843.

Yang, L., Lin, X.S., Gravina, R.J. (2018). Evaluation of dynamic increase factor models for steel fibre reinforced concrete. Construction and Building Materials 190:632–644.

LS-DYNA Support. (R10.0). LS-DYNA user manual R10.0.

Sauer, C., Heine, A., Riedel, W. (2017). Developing a validated hydrocode model for adobe under impact loading. International Journal of Impact Engineering 104:164–176.

Luccioni, B., Isla, F., Codina, R., Ambrosini, D., Zerbino, R., Giaccio, G., Torrijos, M.C. (2018). Experimental and numerical analysis of blast response of High Strength Fiber Reinforced Concrete slabs. Engineering Structures 175:113–122.

Liu, F., Li, Q.M. (2019). Strain-rate effect on the compressive strength of brittle materials and its implementation into material strength model. International Journal of Impact Engineering 130:113–123.

Grote, D.L., Park, S.W., Zhou, M. (2001). Dynamic behavior of concrete at high strain rates and pressures: I. experimental characterization. International Journal of Impact Engineering 25(9):869–886.

Comité Euro-International du Béton. (1993). CEB-FIP model code 1990: design code, Trowbridge, Wiltshire.

Tu, Z.G., Lu, Y. (2009). Evaluation of typical concrete material models used in hydrocodes for high dynamic response simulations. International Journal of Impact Engineering 36(1):132–146.

Kong, X.Z., Fang, Q., Li, Q.M., Wu, H., Crawford, J.E. (2017). Modified K&C model for cratering and scabbing of concrete slabs under projectile impact. International Journal of Impact Engineering 108:217–228.

Wu, P.T. (2019). Study of Static Mechanical Properties of Ultra-High Performance Concrete Under Triaxial Stress States. Master's thesis, Tianjin University, China.

Chen, X.M., Liu, T., Xiao, Z.X. (2012). Numerical Simulation Study of Parameter Sensitivity Analysis on Concrete HJC Model. Chinese Journal of High Pressure Physics 26 (03):313-318.

Jiang, G.P., Jiao, C.J., Xiao, B.Q. (2012). High-pressure state equation of high strength concrete investigated with the gas gun experiment. Acta Physica Sinica 61(2):026701.

Borrvall, T., Riedel, W. (2011). The RHT Concrete Model in LS-DYNA. Proceedings of the 8th European LS-DYNA Conference, Strasbourg, France.

Thomas, R.J., Sorensen, A.D. (2017). Review of strain rate effects for UHPC in tension. Construction and Building Materials 153:846–856.

Hu, A.X., Liang, X.W., Yu, J., Shi, Q.X., Li, L. (2018). Experimental Study of Uniaxial Tensile Characteristics of Ultra-high Performance Concrete. Journal of Hunan University (Natural Sciences) 45(9):30–37.

Lee, M.J., Kwak, H.G., Park, G.K. (2021). An improved calibration method of the K&C model for modeling steel-fiber reinforced concrete. Composite Structures 269:114010.

Li, J., Wu, Q., Chen, X.W., et al. (2017). Numerical study of ultra-high-performance concrete under non-deformable projectile penetration. Construction and Building Materials, 135:447-458.

Lü, Y.Q., Chen, N.X., Wu, H.J., Zhao, H.Y., Zhang, X.Y. (2022). Mechanism of high-velocity projectile penetrating into ultra-high performance concrete target. Acta Armamentarii 43(1):37–47.